Dynamic fluid connectivity during steady-state multiphase flow in a sandstone

Catriona A. Reynolds[a,b,1], Hannah Menke[a,b], Matthew Andrew[c], Martin J. Blunt[a,b], and Samuel Krevor[a,b]

[a]Department of Earth Science and Engineering, Imperial College London, London SW7 2AZ, United Kingdom; [b]Qatar Carbonates and Carbon Storage Research Centre, Imperial College London, London SW7 2AZ, United Kingdom; and [c]Carl Zeiss X-ray Microscopy Ltd., Pleasanton, CA 94588

Edited by David A. Weitz, Harvard University, Cambridge, MA, and approved June 21, 2017 (received for review February 18, 2017)

The current conceptual picture of steady-state multiphase Darcy flow in porous media is that the fluid phases organize into separate flow pathways with stable interfaces. Here we demonstrate a previously unobserved type of steady-state flow behavior, which we term "dynamic connectivity," using fast pore-scale X-ray imaging. We image the flow of N_2 and brine through a permeable sandstone at subsurface reservoir conditions, and low capillary numbers, and at constant fluid saturation. At any instant, the network of pores filled with the nonwetting phase is not necessarily connected. Flow occurs along pathways that periodically reconnect, like cars controlled by traffic lights. This behavior is consistent with an energy balance, where some of the energy of the injected fluids is sporadically converted to create new interfaces.

steady state | pore-scale imaging | immiscible two-phase flow | dynamic connectivity | geologic CO_2 storage

The definition of relative permeability is based on a conceptual model where each phase occupies its own static, connected fraction of the pore space (1–3). Observations of two-phase flow in beadpacks and micromodels at low flow rates show that the wetting- and nonwetting-phase fluids flow through their own network of separate stable pathways. Increasing the saturation of one phase increases the number of channels occupied by one fluid and decreases the number occupied by the other. The nonwetting phase generally occupies the large pores, whereas the wetting phase occupies the small pores and indentations in the surface of the solid (4–7).

When the balance of capillary and viscous forces is modified such that viscous forces begin to dominate at the pore scale, the nonwetting phase can be pushed out of the pore space and flow can occur through the advection of disconnected ganglia (8, 9). The onset of ganglion motion is well understood, and this flow behavior has been observed during steady-state flow in model pore spaces (1–3, 7, 10–13).

The key observation during slow steady-state flow, typical of most displacements in natural settings, such as during hydrocarbon recovery or CO_2 storage, is that the pathway, once established, remains stable (2, 4–7). Flow patterns for different wettabilities have also been quantified in micromodel studies (14). Again, once flow pathways were established, they were not observed to change. However, there are no studies thus far that have investigated this flow behavior in the pore space of natural rocks.

Developments in micro X-ray computed tomography (X-ray CT) mean that pore-scale phenomena can now be observed in rocks at reservoir conditions in both laboratory-based scanners and synchrotron beamlines (8, 9, 15–17). This technological advance has allowed, for instance, observations of residual trapping (18) and wetting behavior (19).

Fast synchrotron tomography allows the acquisition of images in under 60 s. Many unsteady-state, dynamic, pore-scale processes have been imaged, including Haines jumps (15), capillary pressure changes during reservoir condition CO_2-brine drainage (20), ganglion dynamics during the capillary desaturation of oil (21), and reactive transport processes in complex carbonates (22).

These advances in imaging technology have also allowed new pore-scale mechanisms to be identified. At high flow rates, the fragmentation of large trapped ganglia has been observed in the pore space of a complex carbonate rock (23). At lower capillary numbers, the trapping of CO_2 (20) and oil (21) in disconnected ganglia has been quantified in sandstones. The connection and reconnection of ganglia was observed as a result of the local advance and recession of the wetting phase. However, the implications for flow were not quantified, and it was implied that nonwetting-phase displacement occurred by the movement of trapped ganglia through the pore space (21).

Experimental Observations of Steady-State Two-Phase Flow at the Pore Scale

The work presented here is a pore-scale experimental investigation of macroscopic steady-state flow performed at reservoir conditions. We use fast synchrotron X-ray CT to investigate rate-dependent, steady-state two-phase flow behavior at low capillary numbers representative of subsurface flow conditions, well below the threshold for pore-scale ganglion motion, in the pore space of a sandstone. We injected N_2 and brine at a constant fractional flow into a sample of Bentheimer sandstone (apparatus shown in Fig. S1). We altered the capillary–viscous force balance by increasing the total flow rate in a stepwise manner. We demonstrate that flow follows fixed flow paths, as in the traditional theory, but that these pathways have critical connections that are periodically filled with wetting phase, blocking flow.

We define wetting- and nonwetting-phase capillary numbers (7, 10),

$$Ca_w = \frac{v_w \mu_w}{\sigma} \quad [1]$$

Significance

The movement of immiscible fluids through permeable media occurs in many settings, including oil and water flow through rock. Here we present observations of a previously unidentified type of steady-state flow behavior that we term "dynamic connectivity." We demonstrate that flow of the nonwetting phase occurs through a network of connections that continuously rearrange between filled pores. This observation suggests that we need to modify our models of two-phase flow that are fundamental to describing subsurface flow processes such as geologic CO_2 storage and hydrocarbon recovery.

Author contributions: C.A.R. designed research; C.A.R., H.M., and M.A. performed research; C.A.R. and H.M. analyzed data; and C.A.R., H.M., M.A., M.J.B., and S.K. wrote the paper.

The authors declare no conflict of interest.

This article is a PNAS Direct Submission.

Freely available online through the PNAS open access option.

[1]To whom correspondence should be addressed. Email: catriona.reynolds11@imperial.ac.uk.

This article contains supporting information online at www.pnas.org/lookup/suppl/doi:10.1073/pnas.1702834114/-/DCSupplemental.

Table 1. List of experiments

Experiment	Flow Rate,* mL·min^{-1}	Ca_w	Ca_{nw}	Scan time, min	Mean S_{N_2}
1A	0.02	7.00×10^{-7}	2.27×10^{-8}	44	0.274
1B	0.10	3.50×10^{-6}	1.13×10^{-7}	35	0.225
1C	0.30	1.05×10^{-5}	3.40×10^{-7}	45	0.302
1D	0.50	1.75×10^{-5}	5.67×10^{-7}	42	0.321
2A	0.04	1.40×10^{-6}	4.54×10^{-8}	29	0.358
2B	0.30	1.05×10^{-5}	3.40×10^{-7}	28	0.340
2C	1.00	3.50×10^{-5}	1.13×10^{-6}	28	0.354

*Total flow rate, $Q_t = Q_{nw} + Q_w$, where $Q_{nw} = Q_w$.

and

$$Ca_{nw} = \frac{v_{nw}\mu_{nw}}{\sigma}, \quad [2]$$

respectively, where the interstitial fluid velocity (in meters per second) is $v = q/\phi$, q is the Darcy flux, ϕ is the porosity, μ is the dynamic viscosity (in Pascal seconds), and σ is the interfacial tension between the wetting and nonwetting phases (in Newtons per meter).

Coinjection experiments were performed in two sets of increasing total flow rate corresponding to an increasing capillary number (experiments 1A to 1D and 2A to 2C, Table 1), each time starting with the pore space fully saturated with brine. Brine and N_2 were injected at equal flow rates until an approximately constant saturation was established in the core, and then images were acquired over a period of 28 min to 45 min.

The images were processed using the techniques outlined in *Materials and Methods*, using Avizo 9.1 (www.vsg3d.com) to create 3D volumes of N_2 that could be analyzed to assess their volume and connectivity (Figs. S2 and S3). The steady-state saturation of N_2 (Mean S_{N_2}) and the calculated capillary numbers for the wetting and nonwetting phases are given in Table 1.

Connected volumes of N_2 were observed in the low flow rate, low capillary number experiments (1A and 2A). There were no connected pathways of N_2 in experiments 1B to 1D and 2B and 2C, and disconnected ganglia of N_2 of various sizes were present in all of the experiments (Fig. 1).

The ganglia populations were subdivided to make visualizing the connectivity easier (Table S1): large ganglia, which typically contain thousands of pores and may be connected across the field of view (pink volumes, Fig. 1, containing more than 10^7 voxels); medium ganglia, which may be connected over tens to hundreds of pores (blue volumes, Fig. 1, containing 10^5 to 10^7 voxels); and small ganglia, which may be isolated in a single pore or be simply connected over a few pores (green volumes, Fig. 1, containing 5×10^3 to 1×10^5 voxels; ganglia smaller than 5,000 voxels are ignored).

The total saturation throughout each experimental stage remained approximately constant, at a value close to the residual nonwetting phase saturation during imbibition, as measured on larger core samples (24). However, the amount contributed by the different ganglia populations changed with both time and flow rate (Figs. 2 and 3). All of the experiments contained medium and small ganglia, whereas the large ganglia are present only at low flow rates (experiments 1A, 1B, and 2A). As the flow rate rises, the proportion of small and medium ganglia increases, and the proportion of large ganglia decreases.

Large ganglia that are connected across the field of view are only observed for the lowest flow rate experiments (1A and 2A). However, the connected pathway is not stable and varies in both volume and position over time. Changes in connected pathway volume do not correspond to a change in total N_2 saturation, but are the result of splitting the original connected ganglion into two separate large ganglia, or multiple medium ganglia (Fig. 4). Parts of the connected pathway repeatedly disconnect and reconnect, changing the position of the connected pathway in the pore space.

The pathway stability can be described in terms of the number of disconnection events that take place between each time step. A decrease in volume of the connected pathway requires a section to become disconnected, whereas an increase requires a connection with a neighboring ganglion to be made. Increasing the flow rate, or capillary number, results in more disconnection and reconnection events, and the pathway has an increasingly dynamic connectivity.

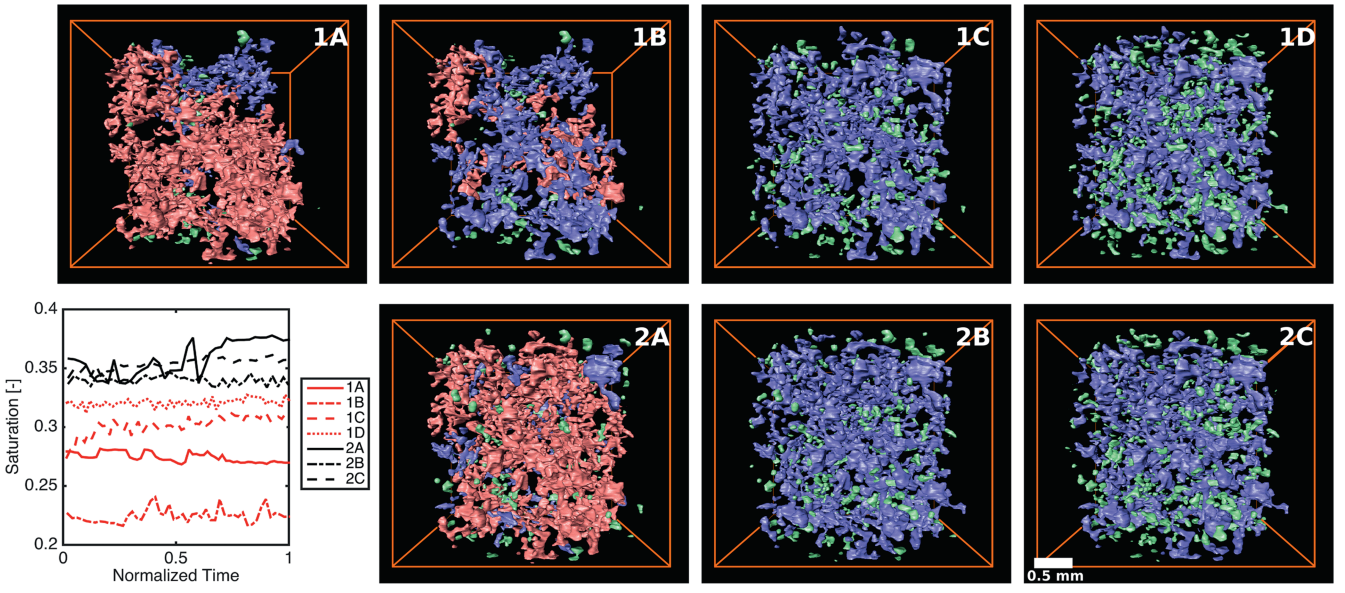

Fig. 1. Ganglia populations contributing to average saturation. Average saturation is plotted versus time, and volume renderings of ganglia at the end of the experiment are shown, for experiments 1A to 1D and 2A to 2C. Ganglia are subdivided by size: large (pink), medium (blue), and small (green). Flow is from top to bottom. Time from the beginning of the experiment is normalized by the total experimental time (Table 1).

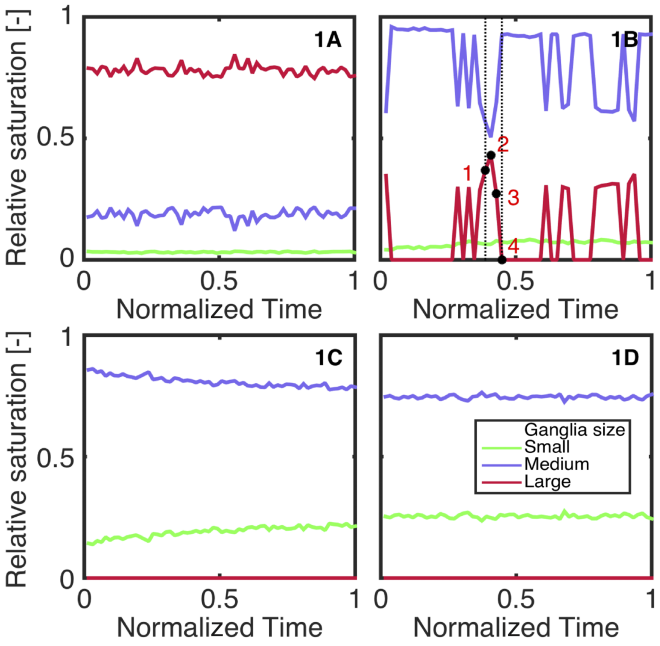

Fig. 2. Interaction between ganglia populations. Plots show the relative saturation of small (green), medium (blue), and large (pink) N_2 ganglia for experiments 1A to 1D.

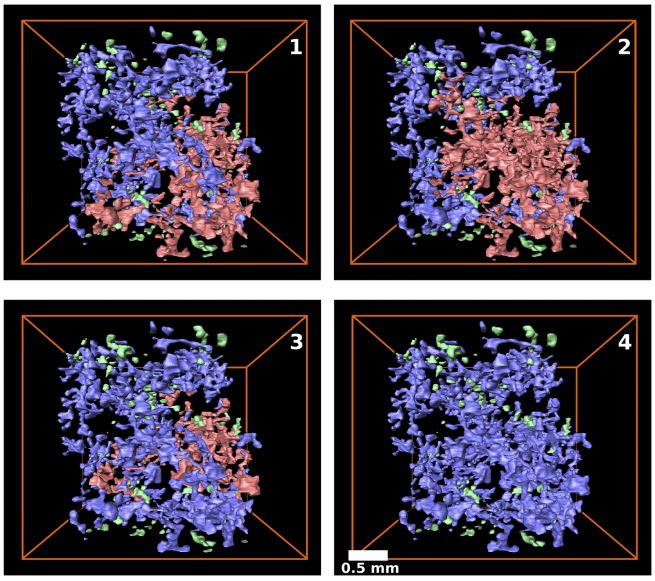

Fig. 3. Interaction between ganglia populations. Volume renderings of ganglia from experiment 1B are shown, corresponding to the numbers in red on Fig. 2.

This dynamic connectivity also occurs in experiments without connected pathways, through the interaction between the ganglia populations (Fig. 2). At very low (experiment 1A) or high (experiments 1C and 1D) flow rates, the proportions of small, medium, and large ganglia stay constant over time. The volume of fluid transported through the pore space during the acquisition of a single image is greater than the total pore volume of the imaged core. Thus, the interfaces between ganglia in the pore space must change for the nonwetting phase to flow. Rearrangement of interfaces means the change in the number of ganglia could be due to the transport of individual ganglia wholesale through the pore space or due to the same dynamic connectivity behavior seen in the connected pathways, in which connections open briefly to create a pathway for fluid migration from one pore to another.

In the time sequence images shown in Fig. 3 (see also Movies S1–S9), individual ganglia moving progressively through the pore space cannot be identified. Instead, the positions of ganglia appear to be static, with some of the connectivity changing between neighboring ganglia. This change in connectivity is illustrated in the subvolume time sequence in Fig. 5. We observe that interaction between ganglia populations is the result of dynamic connectivity in the pore throats, whereas the pore bodies remain filled throughout.

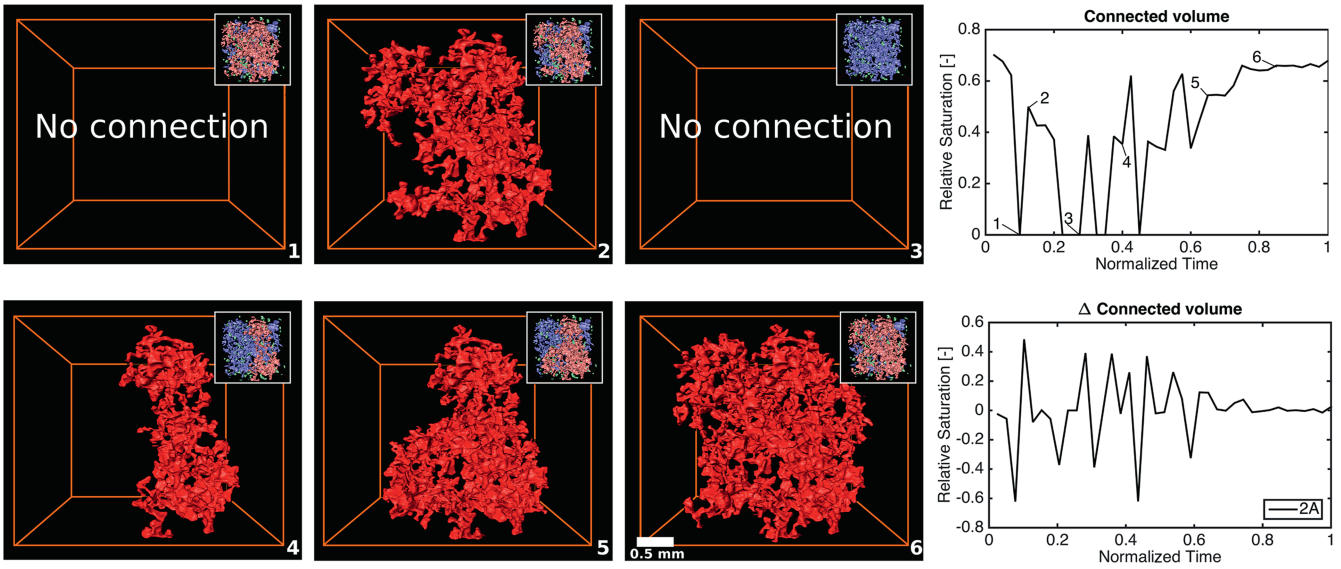

Fig. 4. Volume of N_2 instantaneously connected from inlet to outlet. In graphs, connected volume of N_2 as a percent of total N_2 saturation and the relative change in connected volume with time are plotted for experiment 2A. Images show volume rendering of N_2 for experiment 2A (numbers 1 to 8). The connected volume of N_2 is shown in red. (*Insets*) Ganglia split by size: small (green), medium (blue), and large (pink) ganglia. Flow is from top to bottom.

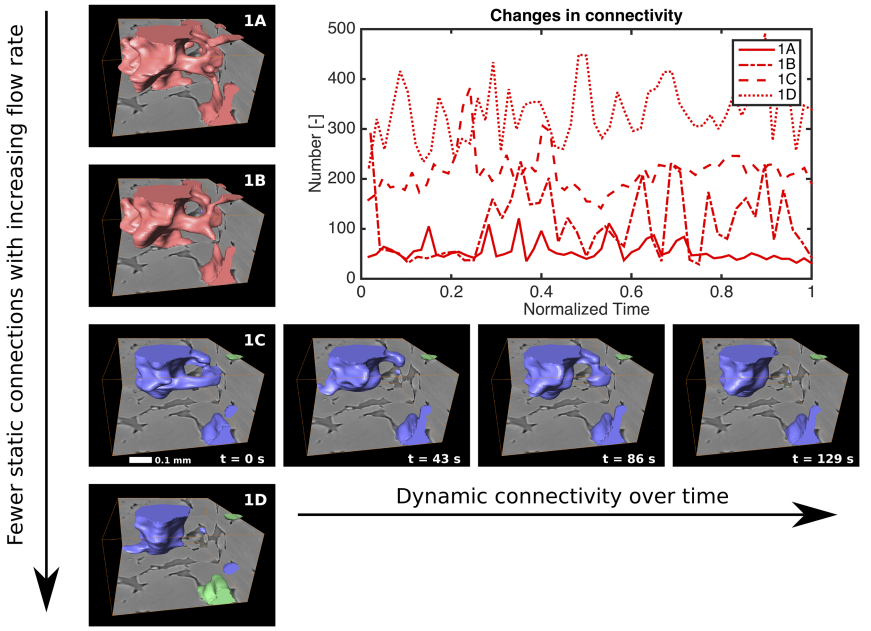

Fig. 5. Change in connectivity with flow rate and time. Volume renderings of N_2 ganglia, colored by size, in a 720 × 720 × 360 μm subvolume are shown for experiments 1A to 1D. Four consecutive time steps are shown for experiment 1C, illustrating two continuously filled pores and several transient branching connections. Also shown is the number of connections through pore throats in the whole imaged volume versus time. The volume of N_2 shown in the images is connected both inside and outside the subvolume.

Dynamic Connectivity: A Single Flow Regime

We estimate that the transition from experiments containing some intermittent connected pathways to experiments containing no connected pathways occurs at critical wetting and critical nonwetting capillary numbers, $Ca_{w,crit} = 4.5 \times 10^{-6}$ and $Ca_{nw,crit} = 8.5 \times 10^{-8}$ (Fig. 6). These are two to three orders of magnitude smaller than the transition identified in beadpack experiments (7); this is likely due to the difference in pore structure between beadpacks and the sandstone used in this study.

However, the dynamic connectivity shown is different from that assumed in the traditional conceptual picture of two-phase flow. Instead of a transition from connected pathways to the advection of discrete ganglia, we see transport of the nonwetting phase through pathways that are largely fixed, with some connections that periodically open and close. This novel flow behavior is separate from that reported by Datta et al. (7, 10), specifically, that the ganglia do not flow but instead rearrange their connectivity between filled pores. As capillary number increases, the frequency of connection and disconnection increases, and thus no connected pathway is ever observed.

Fundamentally, steady-state fluid displacement is controlled by an energy balance (25). Work is done to inject fluids: The power per unit volume expended through fluid movement for either phase is approximately given by $dW/dt = -\mathbf{q_t} \cdot \nabla P \approx \mu q_t^2 / K_{eff}$, where K_{eff} is the effective permeability in multiphase flow and q_t is the total Darcy velocity (26). The surface energy of the interface between the wetting and nonwetting phases per unit volume is $\sim \sigma / l$, where l is a characteristic pore size. The time taken to provide sufficient energy to create the fluid interfaces is roughly $t = \sigma K_{eff} / l \mu q_t^2$. As there is no net displacement in the experiments, fluctuations in the position of the interfaces eventually dissipate the surface energy as heat. For an order of magnitude estimate, we consider $K_{eff} = 10^{-12}$ m^2, $l = 10^{-4}$ m, and $q_t = 2.7 \times 10^{-5}$ m·s^{-1}, with the brine viscosity corresponding to the lowest flow rate experiment in Table 1 (16). We find a timescale for interface creation of 1.4×10^3 s or around 20 min. Thus, between two successive scans (43 s), there is sufficient energy provided by the injection to alter the fluid configuration in only around 3% or the pores, or 160 elements in a scan volume encompassing ∼5,000 pores. Our observations show that this leads to connected flow paths that are only sometimes stable across successive scans. However, at the highest flow rates studied, a 50-fold increase in q_t, or a 2,500-fold change in energy, allows rearrangement in all of the pores between scans, leading to a much more dynamic flow pattern.

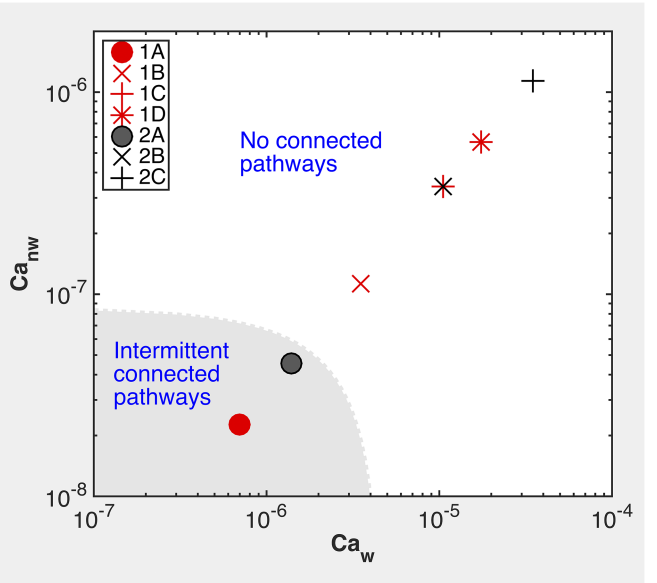

Fig. 6. The arrangement of N_2 (as transient connected pathways or as disconnected ganglia) is shown as a function of wetting and nonwetting phase capillary numbers for experiments 1A to 1D and 2A to 2C. We estimate that no connected pathways form above $Ca_{w,crit} = 4.5 \times 10^{-6}$ and $Ca_{nw,crit} = 8.5 \times 10^{-8}$.

Reconciling Pore-Scale Flow Mechanisms with Continuum-Scale Properties

The dynamic connection and disconnection we have described is a previously unidentified type of ganglion dynamics. Although, instantaneously, we observe discrete ganglia, they are arranged in a pathway. This pathway is comparable to a road network with traffic lights. The flow of cars through the network can be stopped by a red traffic light, blocking a junction for a short time. When the light turns green—when the local energy balance favors movement again—the flow continues down the same road. On the pore scale, this stop and start process appears very different from the continuous pathway flow originally used to justify the extension of Darcy's law to multiple fluid phases. Primary drainage in water-wet rocks is accurately modeled by pore-scale simulations (3). At the large scale, although the N_2 is instantaneously arranged in separate ganglia, the behavior overall is that of a continuous pathway. Thus, when we make continuum-scale measurements such as relative permeability, we measure flow through the entire road network, not the stop and start of an individual car. The conductance of a phase is governed by the entire volume that it occupies, even intermittently, with a correction for the fraction of time that it occupies each pore.

There have been suggestions of dynamic connectivity in some of the earliest observations of two-phase flow in 2D. Chatenever and Calhoun (5) observed channel flow in a single layer of glass beads and noted that "In the case of temporary flow disturbances the flow channels exhibited an elasticity whereby they tended to resume almost their exact starting configurations with the reestablishment of the original steady conditions." In a recent 3D observation, Datta et al. (7) noted that "Intriguingly... sections of this connected 3D pathway intermittently break up into discrete ganglia, several pores in size - the observed break up process occurs irregularly, punctuated by intervals of continuous flow." It is likely that both these observations are the same disconnection and reconnection behavior observed in the pore-scale experiments presented here.

Conclusions

We have performed coinjection microcore floods using N_2 and brine to investigate two-phase steady-state flow behavior at reservoir conditions and have identified a type of flow behavior we term "dynamic connectivity." Connected flow paths of N_2 exist only during low capillary number flow, but are not stable, interacting strongly with the ganglia population in the pore space. At the lowest capillary numbers used, there is sufficient power to reorganize fluid interfaces in up to 3% of the pores over the timescale of observation. This reorganization means connected flow pathways are only stable over tens to hundreds of seconds. The work input increases quadratically with flow rate such that the highest capillary numbers used provide sufficient power for dynamic connectivity to be observed in many of the pores. This intermittency is likely to be initiated by changes in local capillary pressure as fluid interfaces advance. These pressure changes can drive rapid movement and rearrangement of the fluid phases even in a steady-state flow.

Materials and Methods

Core floods were performed with 1.5 mol·kg^{-1} potassium iodide (KI) brine as the wetting phase and N_2 as the nonwetting phase at 10 MPa and 50 °C. Under these conditions, the fluid viscosities were μ_{brine} = 642.2 μPa·s and μ_{N_2} = 20.8 μPa·s, and the interfacial tension was 64 mN·m^{-1} (27–30). The viscosity ratio of 31:1 used here is typical of gas/oil ratios for during gas injection (31). The viscosity ratio for CO_2 injection in saline aquifers is typically 13:1 (32). The capillary number of observations, $10^{-8} < N_c < 10^{-5}$, ranged from those applicable to subsurface flows ($N_c < 10^{-6}$) to high values at which advective ganglia transport has been previously observed (7). Equal reservoir-condition volumes of brine and N_2 were injected at a constant rate into a Bentheimer sandstone composite microcore composed of four short cores with a total length of 4 cm and each with a diameter of 4 mm. The core sample was contained in X-ray transparent core holder with a confining pressure of 2 MPa over the fluid pressure. The sample was imaged during fluid flow at the Diamond Lightsource Synchrotron. The 3D images with a voxel size of 3.6 μm were acquired every 43 s to create a time series. The sample had a porosity of 0.19 and a pore volume of 0.0075 mL, calculated from images of the dry and brine-filled rock. Detailed methods are provided in *Supporting Information*.

ACKNOWLEDGMENTS. The authors acknowledge Dr. Christoph Rau and Dr. Mirian Garcia-Fernandez for their assistance. We also thank the additional members of the experimental team from Imperial College who participated in the experiments. In particular, we recognize the contributions of Dr. Branko Bjeljic and Dr. Kamal Singh. We gratefully acknowledge Diamond Light Source for access to beamline I13, and funding from Qatar Petroleum, Shell, and the Qatar Science and Technology Park. C.A.R. was funded by Engineering and Physical Sciences Research Council Grant 1304506.

1. Muskat M, Meres MW (1936) The flow of heterogeneous fluids through porous media. *Physics* 7:346–363.
2. Dullien FAL (1991) *Porous Media: Fluid Transport and Pore Structure* (Academic, New York).
3. Blunt MJ (2017) *Multiphase Flow in Permeable Media: A Pore-Scale Perspective* (Cambridge Univ Press, Cambridge, UK).
4. Lenormand R, Zarcone C, Sarr A (1983) Mechanisms of the displacement of one fluid by another in a network of capillary ducts. *J Fluid Mech* 135:337–353.
5. Chatenever A, Calhoun JC (1952) Visual examinations of fluid behaviour in porous media - Part I. *J Pet Technol* 4:149–156.
6. Scheidegger AE (1958) *The Physics of Flow Through Porous Media* (University of Toronto Press, Toronto).
7. Datta SS, Dupin JB, Weitz DA (2014) Fluid breakup during simultaneous two-phase flow through a three-dimensional porous medium. *Phys Fluid* 26:062004.
8. Taber JJ (1969) Dynamic and static forces required to remove a discontinuous oil phase from porous media containing both oil and water. *Soc Pet Eng J* 9:3–12.
9. Avraam DG, Payatakes AC (1995) Flow regimes and relative permeabilities during steady-state two-phase flow in porous media. *J Fluid Mech* 293:207–236.
10. Datta SS, Ramakrishnan T, Weitz DA (2014) Mobilization of a trapped non-wetting fluid from a three-dimensional porous medium. *Phys Fluid* 26:022002.
11. Tallakstad KT, et al. (2009) Steady-state, simultaneous two-phase flow in porous media: An experimental study. *Phys Rev E Stat Nonlin Soft Matter Phys* 80: 036308.
12. Erpelding M, et al. (2013) History independence of steady state in simultaneous two-phase flow through two-dimensional porous media. *Phys Rev E Stat Nonlin Soft Matter Phys* 88:053004.
13. Rassi EM, Codd SL, Seymour JD (2011) Nuclear magnetic resonance characterization of the stationary dynamics of partially saturated media during steady-state infiltration flow. *New J Phys* 13:015007.
14. Zhao B, MacMinn C, Juanes R (2016) Wettability control on multiphase flow in patterned microfluidics. *Proc Natl Acad Sci USA* 113:10251–10256.
15. Berg S, et al. (2013) Real-time 3D imaging of Haines jumps in porous media flow. *Proc Natl Acad Sci USA* 110:3755–3759.
16. Blunt MJ, et al. (2013) Pore-scale imaging and modelling. *Adv Water Resour* 51:197–216.
17. Wildenschild D, Sheppard AP (2013) X-ray imaging and analysis techniques for quantifying pore-scale structure and processes in subsurface porous medium systems. *Adv Water Resour* 51:217–246.
18. Andrew M, Bijeljic B, Blunt MJ (2014) Pore-scale imaging of trapped supercritical carbon dioxide in sandstones and carbonates. *Int J Greenhouse Gas Control* 22:1–14.
19. Singh K, Bijeljic B, Blunt MJ (2016) Imaging of oil layers, curvature, and contact angle in a mixed-wet and a water-wet carbonate rock. *Water Resour Res* 52:1716–1728.
20. Andrew M, Menke H, Blunt MJ, Bijeljic B (2015) The imaging of dynamic multiphase fluid flow using synchrotron-based X-ray microtomography at reservoir conditions. *Transp Porous Media* 110:1–24.
21. Rücker M, et al. (2015) From connected pathway flow to ganglion dynamics. *Geophys Res Lett* 42:3888–3894.
22. Menke HP, Andrew MG, Blunt MJ, Bijeljic B (2016) Reservoir condition imaging of reactive transport in heterogeneous carbonates using fast synchrotron tomography - Effect of initial pore structure and flow conditions. *Chem Geol* 428:15–26.
23. Pak T, Butler IB, Geiger S, van Dijke MIJ, Sorbie KS (2015) Droplet fragmentation: 3D imaging of a previously unidentified pore-scale process during multiphase flow in porous media. *Proc Natl Acad Sci USA* 112:1947–1952.
24. Reynolds CA, Krevor S (2015) Characterizing flow behavior for gas injection: Relative permeability of CO_2-brine and N_2-water in heterogeneous rocks. *Water Resour Res* 51:9464–9489.
25. Cueto-Felgueroso L, Juanes R (2016) A discrete-domain description of multiphase flow in porous media: Rugged energy landscapes and the origin of hysteresis. *Geophys Res Lett* 43:1615–1622.
26. Raeini AQ, Blunt MJ, Bijeljic B (2014) Direct simulations of two-phase flow on micro-CT images of porous media and upscaling of pore-scale forces. *Adv Water Resour* 74:116–126.

27. Span R, W LE, Jacobsen RT, Wagner W, Yokozeki A (2000) A reference equation of state for the thermodynamic properties of nitrogen for temperatures from 63.151 to 1000 K and pressures to 2200 MPa. *J Phys Chem Ref Data* 29:1361–1433.
28. Lemmon EW, McLinder MO, Friend DG (2016) *Thermophysical Properties of Fluid Systems*. *NIST Chemistry WebBook: NIST Standard Reference Database*, eds Mallard PJ, W G (Natl Inst Standards Technol, Gaithersburg, MD), Vol 69.
29. Yan W, Zhao GY, Chen GJ, Guo TM (2001) Interfacial tension of (methane+ nitrogen)+ water and (carbon dioxide+ nitrogen)+ water systems. *J Chem Eng Data* 46:1544–1548.
30. Kestin J, Khalifa HE, Correia RJ (1981) Tables of the dynamic and kinematic viscosity of aqueous NaCl solutions in the temperature range 20–150 °C and the pressure range 0.1–35 MPa. *J Phys Chem Ref Data* 10 71–88.
31. Christie MA, Muggeridge AH, Barley JJ (1993) 3D simulation of viscous fingering and wag schemes. *SPE Reservoir Eng* 8:19–26.
32. Boait FC, et al. (2012) Spatial and temporal evolution of injected co_2 at the Sleipner field, North sea. *J Geophys Res* 117:B03309.
33. Taitel Y, Bornea D, Dukler AE (1980) Modelling flow pattern transitions for steady upward gas-liquid flow in vertical tubes. *AIChE J* 26:345–354.
34. Titarenko V, Titarenko S, Withers PJ, De Carlo F, Xiao X (2010) Improved tomographic reconstructions using adaptive time-dependent intensity normalization. *J Synchrotron Radiat* 17:689–699.
35. Kyrieleis A, Ibison M, Titarenko V, Withers PJ (2009) Image stitching strategies for tomographic imaging of large objects at high resolution at synchrotron sources. *Nucl Instrum Methods Phys Res A* 607:677–684.
36. Kyrieleis A, Titarenko V, Ibison M, Connolley T, Withers PJ (2011) Region-of-interest tomography using filtered backprojection: Assessing the practical limits. *J Microsc* 241:69–82.
37. Søreide I, Whitson CH (1992) Peng-Robinson predictions for hydrocarbons, CO_2, N_2, and H_2S with pure water and NaCl brine. *Fluid Phase Equilib* 77:217–240.
38. O'Sullivan TD, Smith NO (1970) Solubility and partial molar volume of nitrogen and methane in water and in aqueous sodium chloride from 50 to 125 °C and 100 to 600 atm. *J Phys Chem* 74:1460–1466.
39. Buades A, Coll B, Morel JM (2008) Nonlocal image and movie denoising. *Int J Comput Vis* 76:123–139.
40. Lanczos C (1950) An iteration method for the solution of the eigenvalue problem of linear differential and integral operators. *J Res Natl Bur Stand* 45:255–282.
41. Schlüter S, Sheppard A, Brown K, Wildenschild D (2014) Image processing of multiphase images obtained via X-ray microtomography: A review. *Water Resour Res* 50:3615–3639.
42. Beucher S (1991) The watershed Transformation applied to image segmentation. *Scanning Microsc Int Suppl* 6:299–314.
43. Jones AC, et al. (2007) Assessment of bone ingrowth into porous biomaterials using MICRO-CT. *Biomaterials* 28:2491–2504.